Soft Pressure Sensor for Underwater Sea Lamprey Detection

Hongyang Shi, *Graduate Student Member, IEEE*, Ian González-Afanador, *Student Member, IEEE*, Christopher Holbrook, Nelson Sepúlveda, *Senior Member, IEEE*, and Xiaobo Tan, *Fellow, IEEE*

***Abstract*—In this paper, an economical and effective soft pressure sensor for underwater sea lamprey detection is proposed, which consists of an array of piezoresistive elements between two layers of perpendicular copper tape electrodes, forming a passive resistor network. With multiplexers, the apparent resistance corresponding to each pixel of the sensing matrix can be measured directly, where the pixel is identified with the row and the column of the respective electrodes. However, this measured two-point resistance is not equal to the actual cell resistance for that pixel due to the crosstalk effect in the resistor network. Since the cell resistance reflects directly the pressure applied on each pixel, the relationship between the cell resistance and the measured two-point resistance is analyzed for a passive matrix of any size. More importantly, several regularized least-squares algorithms are proposed to reconstruct the cell resistance profile from the two-point resistance measurements, with enhanced robustness of the reconstruction in the presence of measurement noises and modeling errors. The proposed pressure sensor is applied to detect the suction attachment of sea lampreys, a devastating invasive species in the Great Lakes region. Experimental results demonstrate that the pressure sensor can successfully capture the rim profile of the lamprey's sucking mouth. Moreover, the performance and computational complexity of the reconstruction algorithms with different regularization functions are compared.**

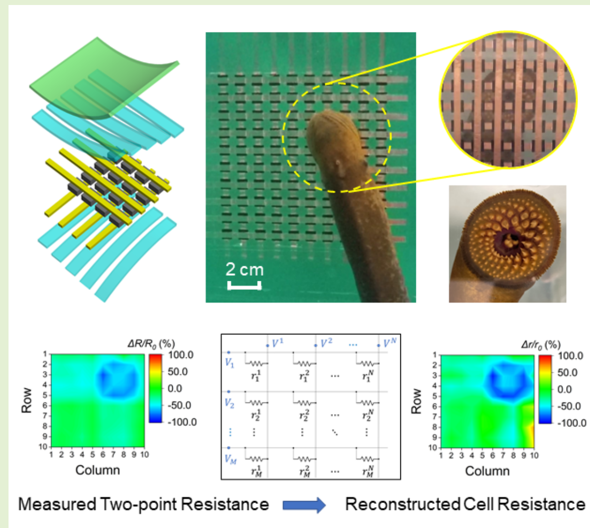

***Index Terms*—Least-squares regularization, resistor network, sea lamprey detection, soft pressure sensor.**

I. Introduction

THE sea lamprey (Petromyzon marinus) in North America is a species of anadromous fish native along the Atlantic coast. After metamorphosis, juvenile sea lampreys with suctorial mouths parasitize host fish, and can kill an estimated 19 kg of fish during their lifetime [1], [2]. The sea lamprey presumably invaded the Laurentian Great Lakes (hereafter Great Lakes) in the early 1900s, and contributed to the collapse of major fish stocks in the Great Lakes [1]. In order to control the sea lamprey invasion and restore the fish community, the Great Lakes Fishery Commission (GLFC) has developed multiple control techniques such as lampricides, barriers, traps, sterile-male-release technique since the 1950s [1], [3]. Recently, selective fish passage has emerged as a high priority for the sea lamprey control program [4], [5], which is designed to allow native and desirable fishes to pass dams while preventing passage of sea lampreys [6], [7].

Real-time detection of adult sea lampreys within or near a fish passage could afford the opportunity to alter fishway operation in response to the detected information. Video analysis has been used or proposed to distinguish some species based on morphological differences [8], [9], but image quality may not be suitable under a broad range of conditions, and image analysis can require massive quantities of data and computationally intensive algorithms.

Manuscript received January 27, 2022; revised April 2, 2022; accepted April 7, 2022. Date of publication April 11, 2022; date of current version May 13, 2022. This work was supported in part by the Great Lakes Fishery Commission under Grant 2018_TAN_54069 and in part by the Michigan State University Strategic Partnership Grant under Grant 16-SPG-Full-3236. The associate editor coordinating the review of this article and approving it for publication was Dr. Yang Yang. *(Corresponding author: Xiaobo Tan.)*

This work involved human subjects or animals in its research. Approval of all ethical and experimental procedures and protocols was granted by the Michigan State University's Institutional Animal Care and Use Committee (IACUC) under Application No. 02/18-028-00.

Hongyang Shi, Ian González-Afanador, Nelson Sepúlveda, and Xiaobo Tan are with the Department of Electrical and Computer Engineering, Michigan State University, East Lansing, MI 48824 USA (e-mail: shihong1@msu.edu; gonza834@msu.edu; sepulve6@msu.edu; xbtan@egr.msu.edu).

Christopher Holbrook is with the U.S. Geological Survey, Great Lakes Science Center, Hammond Bay Biological Station, Millersburg, MI 49759 USA (e-mail: cholbrook@usgs.gov).

This article has supplementary downloadable material available at https://doi.org/10.1109/JSEN.2022.3166693, provided by the authors.

Digital Object Identifier 10.1109/JSEN.2022.3166693

A. Review of Relevant Sensing Methods

Attachment by oral suction is a prominent characteristic of sea lampreys among freshwater fishes in the Great Lakes [10]. They not only rely on oral suction to parasitize other fishes, but frequently attach to artificial and natural substrates (like rocks) during upstream migration and nest building. This trait could be utilized to develop the real-time detection system. The suction mechanism of sea lampreys is illustrated in Adams' thesis [11], and the suction pressure dynamics (pressure amplitude, duration, and pattern of suction events) and pressure distribution across the suctorial mouth are characterized in our previous work using a pressure sensing system based on commercial vacuum sensors [12]. However, the latter sensing technique requires drilling holes on the substrate and using tubes to transmit suction pressures, which are not feasible for large-scale deployment in field environments. Interdigitated electrode (IDE) contact sensors [13] have recently been utilized for sea lamprey detection, with characteristic responses when a lamprey attaches to the sensor. However, IDE sensors do not provide sufficiently granular information such as the suction strength. Soft stretchable sensors [14]–[18] made of elastomers with conductive hydrogels or nanomaterials can measure pressure/stress/strain. Nevertheless, most of the applications are limited to compressive load or tensile stretch and do not respond to a suction stimulus.

During the past decade or so, pressure sensors with highly sensitive and flexible characteristics have been reported with applications in electronic skins for health or motion monitoring [19]–[32], soft robotics [33], [34] and human-machine interface [35], [36]. Multiple designs of the active layer that deforms under pressure and generates changes in the output signal of the capacitive [19]–[23], [33], [37], piezoelectric [24]–[29], and piezoresistive pressure sensors [30]–[32], [34], [35], [39], have been proposed to improve the sensor's performance including sensitivity, dynamic range, and response time. These designs include, for example, micro-pyramids [23], micro-protrusion [36], micropores [31], [35], microcracks [39], and nanofibers [20], [25], [30]. Most of these pressure sensors are fabricated with separate layers that are stacked together without any bonding, and are mainly used for measuring compressive pressure, while their performance under negative pressure (e.g., suction) has not been reported in the literature but could have a high possibility of failure due to layers' delamination under suction. Capacitive pressure sensor arrays with an air-gap and diaphragm design is demonstrated to be effective for both positive and negative pressure measurements [37], [38], but capacitive sensors exhibit not only pressure response during contact but also proximity response for the non-contact mode because of the fringe effect [40]. Furthermore, electromagnetic interference (EMI) becomes severe for underwater animal tests since water and animal tissues are both conductive. This interference will cause difficulty in extracting the actual contacting profile unless sophisticated EMI shielding [41] layers are integrated with the sensor devices. On the other hand, piezoelectric pressure sensors only respond well to dynamic change of pressure and are not particularly effective for quasi-static pressure sensing.

Among resistive pressure sensors, the low-cost pressure sensitive film called Velostat [42]–[48], comprised of carbon-impregnated polyolefin and exhibiting piezoresistive property, has been widely investigated in applications such as finger gesture recognition [42], human grasp monitoring [43], foot pressure measurement [44], sitting posture monitoring [45], and prosthetic in-socket pressure sensing [46]. Most of the reported sensor devices consist of a single Velostat film between two conductive tapes or between two layers of orthogonal conductive threads, which show good performance under compressive loads, but would potentially fail when delamination happens under suction. Another idea is to encapsulate individual Velostat film matrix between two layers of perpendicular electrodes [48], where a resistor network forms in the circuit, which introduces the crosstalk issue between adjacent resistors; that is, the measured two-point resistance is influenced by all the other resistors in the network. The relation between the cell resistance at any pixel and the apparent resistance between the two electrodes (i.e., corresponding column and row) is analytically derived in [49], [50], expressed as an explicit nonlinear forward function from the Laplacian matrix of the cell conductance to the measured two-point resistance matrix. Nevertheless, the inverse problem is intractable and no analytical solution is available, and if there are modelling errors or measurement noises, the solution could be unbounded. More importantly, if the measured two-point resistance is used to characterize the pressure response, the sensing matrix devices of different row and column dimensions will show different amplitudes of changes at the same corresponding pixels under the same pressure, due to the crosstalk, which will be problematic for pressure characterization. Therefore, a general method for reconstructing the cell resistance from the measured two-point resistance is needed for practical, versatile applications.

Some researchers studied the circuit hardware and proposed to place diodes as current barriers to avoid crosstalk [48], but this will make the fabrication more complex and leave the sensing panel unsmooth for attachment. Other researchers analyzed the crosstalk error with circuit simulation [51], [52] and proposed numerical algorithms such as fixed-point iteration to calculate the cell conductance from the measured conductance [53]. The fixed-point algorithm unexpectedly generated negative conductance values, which were then directly replaced with zeros in [53]. However, this often leads to unreasonable and potentially misleading interpretations. The least-squares method was also mentioned in [53]; however, the ill-posed nature of the inversion was not accounted for and a small amount of noise on the data could significantly skew the solution [54], [55].

B. Contributions of This Paper

In this work, an economical and effective soft piezoresistive pressure sensing system is developed and applied to sea lamprey detection, and several novel regularization-based methods for reconstructing the cell resistance are proposed and demonstrated in the system. In particular, the proposed pressure sensing panel consists of an array of individual Velostat cells between two layers of orthogonal copper tape electrodes, which forms a passive resistor network, with waterproof encapsulation around the sensing panel. As demonstrated in experiments, this new design greatly mitigates the overall layer delamination problem for the underwater suction scenario. Compared with the field-effect transistor (FET)-pressure sensitive rubber (PSR) devices capable of mapping pressure developed in [56]–[58] that adopt an active matrix design and measure individual pixels without crosstalk, this work addresses the key signal processing challenge arising due to the intrinsic crosstalk issue in a coupled resistor network. Note that, since the passive resistive matrix approach is typically more compact and enables simpler fabrication and measurement than the active matrix approach, pressure sensors based on passive matrices are of great interest.

For the cell resistance reconstruction, this work derives the general relationship between the cell resistance and the measured resistance based on Kirchhoff's current law. We note that, while the mapping from a passive matrix was also discussed in [15], our method is distinct and applicable to a resistive network of any size. In contrast, the work in [15] only considered two special cases: a 2-by-2 and a 3-by-3 resistor network. Their approach therein cannot be readily extended to a network of general size, and unlike our automated scanning process for measurement, it requires significant changes in circuit wiring in the measurement process. More importantly, inspired by the Tikhonov regularization technique for solving inverse problems such as electrical impedance tomography (EIT) [55], [59], we propose regularized least-squares algorithms and examine multiple choices for the penalty function. Four novel compound minimization criteria are explored, where *a priori* terms penalizing a) the cell resistance, b) the relative change in cell resistance, c) the gradient of cell resistance, and d) the gradient of relative change in cell resistance, respectively, are added to the least-squares term to form the cost functions. The reconstruction performance and computational time of these regularization methods in processing data from sea lamprey experiments are compared and discussed. We note that, while it is applied to lamprey detection in this work, the proposed soft piezoresistive pressure sensing system, including the reconstruction algorithms, holds strong promise for numerous other soft robotic systems and electronic skin applications, such as foot pressure sensing, haptic interaction, and soft robotic fingers with haptic feedback.

The rest of the paper is structured as follows. Section II describes the sensor design and fabrication process. The crosstalk issue in the 2D-resistor network and the forward problem relating the cell resistance to the measured two-point resistance are presented in Section III. The reconstruction algorithms for solving the inverse problem are discussed in Section IV. Experimental procedures for testing the sensing system in sea lamprey detection are presented in Section V. Results obtained on directly measured two-point resistance data and on estimated cell resistance distributions reconstructed via different algorithms are shown and discussed in Section VI. Concluding remarks are provided in Section VII.

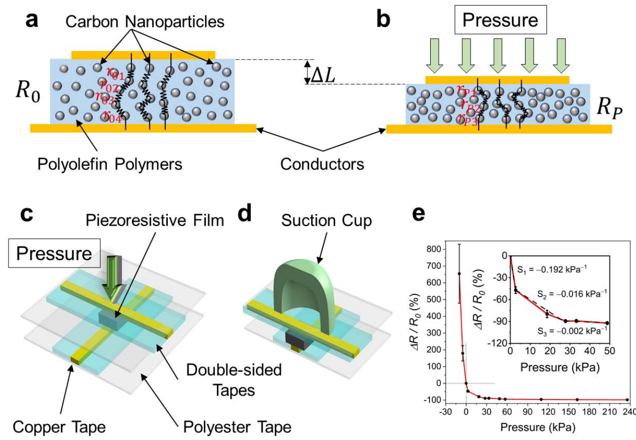

Fig. 1. Working mechanism of the soft pressure sensor and characterization of a single-pixel sensor device. (a) The soft pressure sensor in the initial relaxed state, which shows an initial resistance of R_0 between the top and bottom conductors, and (b) the pressure sensor under compressive pressure, showing a new resistance R_P. (c) The soft pressure sensor with a piezoresistive film between two perpendicular copper tape electrodes under a compressive load, (d) the sensor under a suction cup to test negative pressure response, and (e) the average relative change in resistance (along with the standard deviation) of the single-pixel sensor versus pressure when tested on a flat substrate.

II. Sensor Design and Fabrication

A. Working Principle and Characterization

To fabricate piezoresistive pressure sensor devices, the force-sensitive conductive film 1700 series (SCS company) is used in this work. This film is opaque, volume-conductive carbon-impregnated polyolefin, which has a thickness of 102 μm and a volume resistivity of less than 500 ohm·cm. Since the conductive carbon nanoparticles are embedded in the non-conductive polyolefin polymers, as shown in Fig. 1-a, the film exhibits a high resistance in the initial state. When the film is under external compressive force or pressure (Fig. 1-b), the carbon nanoparticles will get closer, which results in a lower resistance. The resistance change directly reflects the magnitude of the external compressive pressure, and this property can be used for piezoresistive pressure sensing.

To start from a single-pixel soft pressure sensor, a 6 mm $\times$ 6 mm piezoresistive film is between two cross-bar copper tape electrodes (100 mm $\times$ 3 mm $\times$ 0.04 mm) with polyester tape and double-sided tapes for adhesion. Fig. 1-c shows the soft sensor under a compressive pressure, while Fig. 1-d shows the sensor under suction pressure via a suction cup. Two single-pixel pressure sensors were characterized with different loads and suction pressures, with each pressure tested for three rounds individually. The response results were averaged, and the characterization curve of relative change in measured resistance $\Delta R/R_0$ vs. pressure P (-10∼235 kPa) is shown in Fig. 1-e. When the compressive load reaches 235 kPa, the resistance decreased by 98%. On the other hand, when the suction pressure was set to -10 kPa, the resistance increased by about 654%, likely due to local delamination upon suction, although the delamination has been greatly mitigated by this structure design and fabrication method.

$\Delta R/R_0$ decreases linearly with the applied pressure in the low pressure region. The pressure sensitivity, $S = \delta(\Delta R/R_0)/\delta P$, indicates the local slope in the response

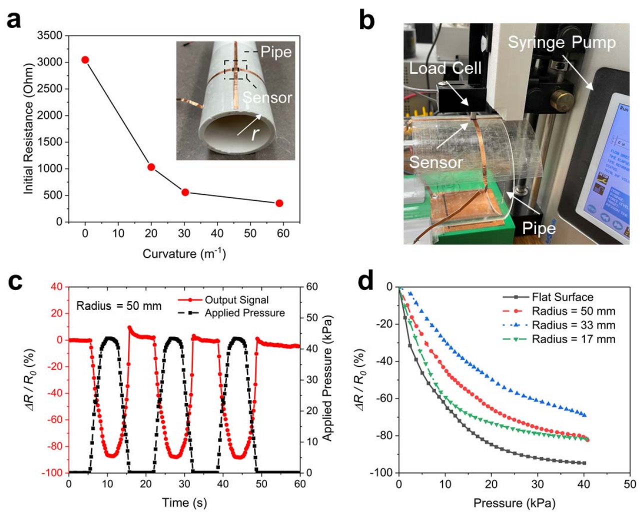

Fig. 2. Performance of the soft pressure sensor device under different bending conditions. (a) The initial (unloaded) resistance of the single-pixel pressure sensor at different curvature radii. (b) The experimental setup for loading pressure on the sensor on curved surfaces. (c) Time-resolved measurements of the output signal for an applied pressure with three rounds of loading and unloading processes on a curved surface with radius 50 mm. (d) Pressure response comparison of the single-pixel sensor at different curvature radii with an applied pressure up to 40 kPa.

curve. The inset of Fig. 1-e shows the variation of the sensitivity depending on the applied pressure: an S value of -0.192 kPa^{-1} between 0 and 2.5 kPa, which reduces to about -0.016 kPa^{-1} for pressure between 2.5 and 28 kPa. When the pressure is above 28 kPa, the relative change in resistance seems to be largely saturated and not to decrease appreciably with pressure.

To investigate the mechanical flexibility such as bending deformation of this soft sensor, we examined a single-pixel sensor's resistance when the sensor device was bent. Fig. 2-a shows the resistance of the sensor when it was bent and attached onto curvy surfaces. The initial (unloaded) resistance was maximum at on a flat surface (zero curvature with a value about 3.05 kΩ), and then decreased to about 1.03 kΩ, 560 Ω, and 350 Ω at a curvature of 20 m^{-1}, 30.3 m^{-1}, and 58.8 m^{-1}, respectively, which demonstrates the significant dependence of the initial resistance on the curvature. The reason for this change in the initial resistance is that larger curvature implies higher bending stress in the sensor device, which leads to greater compression between the electrodes and causes a drop in resistance. To shed light on the pressure response of the sensor device on curvy surfaces, time-resolved measurements were further conducted. As shown in Fig. 2-b, a program-customized syringe pump (Legato 110, KD Scientific, Inc.) was used to apply an external pressure of up to about 40 kPa onto the bending sensor (effective pressure contact area of 3 mm $\times$ 3 mm from the copper electrodes) attached on a pipe, where the pressure was calculated based on the measured contact force through a load cell (GS0-100, Transducer Techniques, LLC). Three cycles of loading and unloading processes were repeated with a period of approximately 18 s. Fig. 2-c shows the relative change in the resistance, $\Delta R/R_0$, of the sensor for the case with curvature radius of 50 mm, where, $\Delta R = R - R_0$, R_0 is the initial resistance at the bending status, and R is the new resistance under the external pressure. During these three rounds of tests, the sensor was repeatable and robust. Furthermore, for different curvature radii (50 mm, 33 mm, and 17 mm), the pressure response curves of the same sensor device are plotted in Fig. 2-d for comparison. Clearly, the relative change in resistance exhibits maximal values at 40 kPa, achieving -94% when the sensor device is on the flat substrate, then it reduces to -82%, -69%, and -81% on the curvy surface with a curvature radius of 50 mm, 33 mm and 17 mm, respectively. The maximum (absolute) change in the resistance output for these curvy cases drops since the initial resistance of the sensor under bending on the curvy surfaces is much smaller than that on the flat substrate.

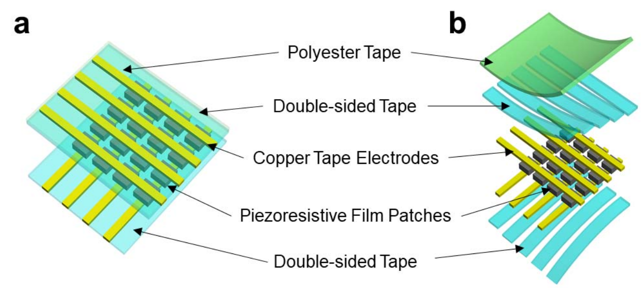

Fig. 3. Schematic of a 4-by-4 piezoresistive pressure sensing matrix. (a) The bonding status of all layers, and (b) the exploded view.

B. Sensor Matrix Structure and Fabrication Process

The structure of the proposed conductive film-based pressure sensor (4-by-4 matrix for schematic illustration) is shown in Fig. 3, where individual conductive film patches were distributed uniformly and encapsulated between two layers of copper tape electrodes. Note that in order to have reliable resistance measurement, a good and stable contact between the surfaces of the conductive film patches and the copper tapes needs to be guaranteed. In this work, we used double-sided acrylic tapes and one-sided polyester tape to bond the layers. With more individual piezoresistive film patches embedded into the matrix, a larger resistor network with M rows and N columns of pixels will be formed, which will be discussed in the modeling section.

Fig. 4 shows the fabrication process for a 10 $\times$ 10 pressure-sensing matrix with a sensing area of 10 $\times$ 10 cm^2. First, 10 pieces of 15 cm $\times$ 3 mm $\times$ 0.04 mm (length $\times$ width $\times$ thickness) copper foil tapes and 11 pieces of 15 cm $\times$ 6.3 mm $\times$ 0.04 mm (length $\times$ width $\times$ thickness) double-sided acrylic tapes were adhered side by side in an alternating manner onto a 300 mm $\times$ 300 mm $\times$ 3 mm acrylic plate; each copper tape has two double-sided tapes bordering on both sides. Then the conductive piezoresistive film was cut into one hundred pieces of square patches (each measuring 6 mm $\times$ 6 mm), which were placed uniformly on the copper tapes as individual piezoresistive sensors. Here, the copper tapes would work as the column electrodes with the double-sided acrylic tapes serving two purposes: filling the space between the copper tapes (thus making the entire bottom layer flat) and fixing the edges of the conductive film patches

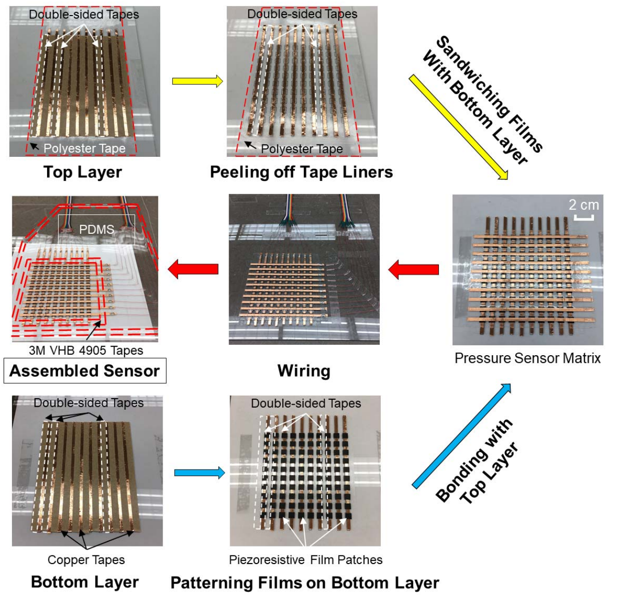

Fig. 4. Fabrication process of the 10-by-10 soft pressure sensing matrix. The paper liners of the double-sided tapes were not peeled off in the top left and bottom left pictures, but were peeled off in the following steps. Picture of the final fabricated 10-by-10 pressure sensing panel with PDMS (polydimethylsiloxane) waterproof encapsulation. The red dashed lines show the edges of the mold formed by 3M VHB 4905 tapes, while the white bounding box titled "PDMS" shows the PDMS encapsulation layer between the inner and outer 3M VHB 4905 tape boundaries.

(which was why the patch was wider than the copper tape). The shiny and non-adhesive surfaces of all the copper tapes were exposed outwards in order to contact the conductive film patches since the adhesive side of the copper tape was not prominently conductive.

Similarly, another 10 pieces of copper foil tapes and 11 pieces of double-sided acrylic tapes were attached onto the adhesive side of a 10 cm $\times$ 20 cm polyester tape, which would work as the top layer of the pressure sensing panel. Then the top layer was rotated by 90°C and put upside down to attach onto the bottom layer, with the conductive film patches between the top and bottom layers of copper tape electrodes. These two layers of copper electrodes would serve as the address lines of the sensing panel. The panel was then pressed with caution in order to form a stable bonding around each pixel between the adhesive layers. After that, each copper tape was connected with a jumper wire by soldering as the circuit extension for measurements. Finally, in order to be able to deploy the pressure sensing panel underwater, waterproof encapsulation by polydimethylsiloxane (PDMS, with a 10:1 wt.% mixing ratio of PDMS base: curing agent) was achieved around the sensing panel, where the red dash lines show the edges of the 3M VHB 4905 double-sided tapes (3 layers bonded together, with a thickness of 1 mm for each layer) attached on the panel which were used to form a mold for the PDMS liquid before curing.

III. Modeling of the Resistor Network

A. The 2D Resistor Network

For the M-by-N 2D resistor network shown in Fig. 5, two multiplexers are used to select the column and the row to form the circuit for a given "pixel". By using a voltage divider with a reference resistor R_{ref}, the resistance measurement R_j^k between the selected j th row and k th column can be calculated as:

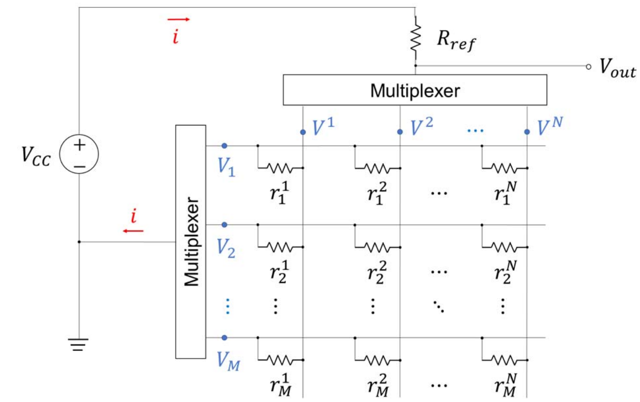

Fig. 5. Schematic of the M-by-N resistor network and the voltage-divider circuits for resistance measurement.

$$R_j^k = \frac{V_{out}}{V_{cc} - V_{out}} R_{ref} \tag{1}$$

Note, however, that the measured two-point resistance R_j^k is not equal to the cell resistance r_j^k at that pixel (j, k) due to crosstalk; in particular, R_j^k is theoretically smaller than r_j^k since it is a parallel connection between r_j^k and a network of resistors between row j and column k. For instance, if row 1 and column 1 are selected by the multiplexers, the current would be injected from node V^1 to V_1 through cell resistor r_1^1 and other branches; for example, the current could flow from node V^1 to V_2 through r_1^2, then to V^2 through r_2^2, and finally back to V_1 through r_2^1. With larger dimensions of the network, there will be more circuit loops involved between the selected row and column.

B. Mapping Contours Based on Measured Resistance

With the fabricated 10 $\times$ 10 soft pressure sensor array, using two 16-channel multiplexers (SparkFun CD74HC4067) and a 1k ohm reference resistor, the two-point resistance between each row and each column could be measured directly through the voltage divider circuit given in Fig. 5. A series of experiments were conducted on the 10 $\times$ 10 soft pressure sensor array, such as the loading of an aluminum rod (Fig. 6-a), the loading of weight through a 3D-printed ring part (Fig. 6-b), the suction and attachment of a suction cup under different negative pressures in air (Fig. 6-c,d), and also the suction cup experiments with the soft pressure sensor matrix under water in a tank (Fig. 6-e,f). All the mapping contours of relative change in directly measured resistance are shown side-by-side with the corresponding experimental picture, which demonstrates that this soft pressure sensor can successfully detect multiple kinds of pressure patterns.

C. Formulation of the Forward Problem

It is of interest to find the relation between the cell resistance values $\{r_j^k\}$ and the measured resistance values $\{R_j^k\}$, which is needed in the reconstruction algorithms. To derive this relationship, nodal analysis or the branch current method is used in this work. In nodal analysis one equation is given at each node, requiring that the branch currents incident at a node must sum to zero based on the Kirchhoff's current law (KCL). Once the branch currents are expressed in terms of the circuit node voltages, the conductance between any two nodes could be discovered.

In general, for the $M \times N$ resistor network in Fig. 5, if the voltage source is replaced with a current source, M voltage nodes for the rows and N voltage nodes for the columns can be studied; correspondingly, $(M+N)$ current sources (including possibly zero current) would be present at these $(M+N)$ nodes. According to KCL, the node-voltage equations can be written in a matrix form as:

$$\boldsymbol{L}\boldsymbol{V} = \boldsymbol{I} \tag{2}$$

$$\boldsymbol{L} = \begin{bmatrix} C_{1,1} & \cdots & C_{1,M} & C_1^1 & \cdots & C_1^N \\ C_{2,1} & \cdots & C_{2,M} & C_2^1 & \cdots & C_2^N \\ \vdots & \ddots & \vdots & \vdots & \ddots & \vdots \\ C_{M,1} & \cdots & C_{M,M} & C_M^1 & \cdots & C_M^N \\ C_1^1 & \cdots & C_M^1 & C^{1,1} & \cdots & C^{1,N} \\ C_1^2 & \cdots & C_M^2 & C^{2,1} & \cdots & C^{2,N} \\ \vdots & \ddots & \vdots & \vdots & \ddots & \vdots \\ C_1^N & \cdots & C_M^N & C^{N,1} & \cdots & C^{N,N} \end{bmatrix} \tag{3}$$

$$\text{and } \boldsymbol{V} = \begin{bmatrix} V_1 \\ V_2 \\ \vdots \\ V_M \\ V^1 \\ V^2 \\ \vdots \\ V^N \end{bmatrix}, \quad \boldsymbol{I} = \begin{bmatrix} I_1 \\ I_2 \\ \vdots \\ I_M \\ I^1 \\ I^2 \\ \vdots \\ I^N \end{bmatrix} \tag{4}$$

where, $\boldsymbol{L}_{(M+N)\times(M+N)}$ is the Laplacian matrix of the $M \times N$ resistor network, $\boldsymbol{V}$ is the voltage pattern, and $\boldsymbol{I}$ is the current pattern. $C_{j,j}$ is the sum of the conductance between the row node V_j and any other node; $C^{k,k}$ is the sum of the conductance between the column node V^k and any other node; C_j^k is the negative of the sum of the conductance between the row node V_j and the column node V^k; $C_{j,h} = 0$, where $1 \le j \ne h \le M$, is the conductance between row j and row h; and $C^{k,l} = 0$, where $1 \le k \ne l \le N$, is the conductance between column k and column l, since the rows are not connected directly with each other and neither are the columns. $\boldsymbol{L}$ is singular since the sum of all rows of $\boldsymbol{L}$ is equal to 0, which means these $(M+N)$ equations are not independent [40]. To remove the redundant equation, the first row node can be chosen as the ground (zero voltage reference), $V_1 = 0$, and the first equation in Equation (2) can be eliminated. Then a new cofactor matrix with a reduced dimension of $(M+N-1) \times (M+N-1)$ along with $(M+N-1)$ independent equations can be obtained from the Laplacian matrix, and Equation (2) is reduced to

$$\mathbb{C}\mathbb{V} = \mathbb{I} \tag{5}$$

where,

$$\mathbb{C} = \begin{bmatrix} C_{2,2} & \cdots & C_{2,M} & C_2^1 & \cdots & C_2^N \\ C_{3,2} & \cdots & C_{3,M} & C_3^1 & \cdots & C_3^N \\ \vdots & \ddots & \vdots & \vdots & \ddots & \vdots \\ C_{M,2} & \cdots & C_{M,M} & C_M^1 & \cdots & C_M^N \\ C_2^1 & \cdots & C_M^1 & C^{1,1} & \cdots & C^{1,N} \\ C_2^2 & \cdots & C_M^2 & C^{2,1} & \cdots & C^{2,N} \\ \vdots & \ddots & \vdots & \vdots & \ddots & \vdots \\ C_2^N & \cdots & C_M^N & C^{N,1} & \cdots & C^{N,N} \end{bmatrix}$$

$$= \begin{bmatrix} \sum_{j=1}^{N} g_2^j & 0 & 0 & -g_2^1 & \cdots & -g_2^N \\ 0 & \ddots & 0 & \vdots & \ddots & \vdots \\ 0 & 0 & \sum_{j=1}^{N} g_M^j & -g_M^1 & \cdots & -g_M^N \\ -g_2^1 & \cdots & -g_M^1 & \sum_{i=1}^{M} g_i^1 & 0 & 0 \\ \vdots & \ddots & \vdots & 0 & \ddots & 0 \\ -g_2^N & \cdots & -g_M^N & 0 & 0 & \sum_{i=1}^{M} g_i^N \end{bmatrix} \tag{6}$$

$$\text{and } \mathbb{V} = \begin{bmatrix} V_2 \\ V_3 \\ \vdots \\ V_M \\ V^1 \\ V^2 \\ \vdots \\ V^N \end{bmatrix}, \quad \mathbb{I} = \begin{bmatrix} I_2 \\ I_3 \\ \vdots \\ I_M \\ I^1 \\ I^2 \\ \vdots \\ I^N \end{bmatrix} \tag{7}$$

Here, $\mathbb{C}$ is non-singular, and $g_j^k = \frac{1}{r_j^k}$ is the conductance of the cell resistor r_j^k. One can then obtain

$$\mathbb{V} = \mathbb{C}^{-1}\mathbb{I} \tag{8}$$

If all cell resistances $\{r_j^k\}$ are known, the co-factor matrix $\mathbb{C}$ is available and so is its inverse. The current pattern $\mathbb{I}$ can be specified in this way: for the current loop between the studied row node V_j and the column node V^k, since the current source noted as i is injected into the column node V^k, the corresponding current element $I^k = i$; and since the current is withdrawn from the row node V_j to the ground, the corresponding current element $I_j = -i$; and all the other row and column nodes have zero current sources. For instance, if the column node V^1 (flow in) and the row node

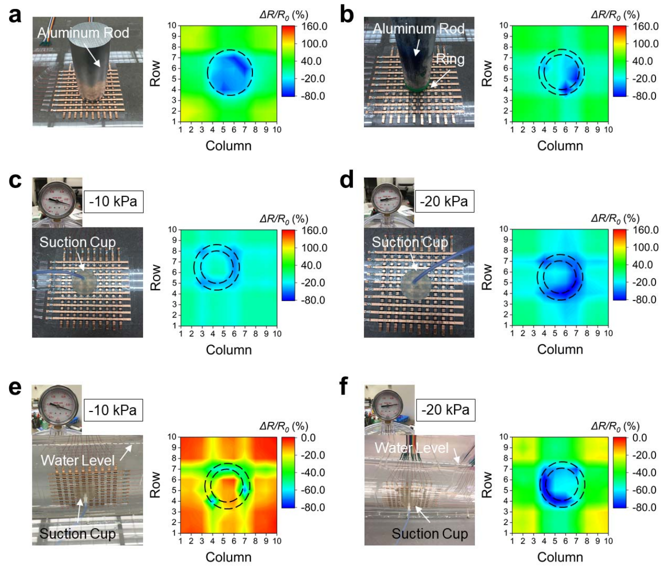

Fig. 6. Mapping contours of the soft pressure sensing matrix based on relative change in directly measured resistance with the following experimental conditions: (a) a ϕ40 mm (ϕ represents diameter), 680 g aluminum rod was loaded on the sensing matrix, (b) a ϕ27 mm $\times$ ϕ35 mm $\times$ 5mm 3D printed ring part under a 850 g aluminum rod was loaded on the sensing matrix, (c) -10 kPa and (d) -20 kPa, respectively, negative pressure was applied on the sensing matrix via a ϕ27 mm $\times$ ϕ35 mm PDMS suction cup in air, and (e) -10 kPa and (f) -20 kPa, respectively, negative pressure was applied on the sensing matrix via the same suction cup under water, where the top row of copper tape electrode of the soft pressure sensor was about 7 cm lower than the water level.

V_2 (flow out) are the two points to measure the resistance, the current pattern $\mathbb{I} = \left[I_2\ I_3 \cdots I_M\ I^1\ I^2 \cdots I^N\right]^T = \left[-i\ 0 \cdots 0\ i\ 0 \cdots 0\right]^T$. If V^1 (flow in) and V_1 (flow out) are the two points to measure the resistance, then the current pattern $\mathbb{I} = \left[0\ 0 \cdots 0\ i\ 0 \cdots 0\right]^T$.

Based on Equation (8), the voltages at all the nodes can be expressed in terms of the current i, and thus according to Ohm's Law, the two-point resistance R_j^k between the studied row V_j and column V^k can be solved as:

$$R_j^k = \frac{V^k - V_j}{i} \tag{9}$$

With Equations (5)-(8), there exists an implicit function $\boldsymbol{f}(\cdot)$ mapping from the cell resistance matrix $\boldsymbol{r} = \left[r_j^k\right]$ to the measured two-point resistance matrix $\boldsymbol{R} = \left[R_j^k\right]$:

$$\boldsymbol{R} = \boldsymbol{f}(\boldsymbol{r}) \tag{10}$$

The algorithm for computing $\boldsymbol{R}$ using $\boldsymbol{r}$ is given in Supporting Information Algorithm 1. Note that in reality the measured two-point resistance matrix, $\boldsymbol{R_m}$, is not exactly equal to $\boldsymbol{R}$ as calculated in Equation (10), due to modeling errors and measurement noises.

Although Equation (5) is linear in the cell conductance, the mapping from the cell conductance to the cell resistance is reciprocal and nonlinear. And since $C_{j,j}$ and $C^{k,k}$ are the sums of the conductance connected to the same row or column node, respectively, Equation (10) for the forward problem is nonlinear and implicit. In the next section we present algorithms for solving the inverse problem.

IV. Cell Resistance Reconstruction via Least-Squares Regularization

As discussed in the previous section, the forward problem from the cell resistance matrix $\boldsymbol{r}$ to the measured resistance matrix $\boldsymbol{R}$ is relatively straightforward. However, the inverse problem, which is reconstructing the cell resistance $\boldsymbol{r}$ based on the measured two-point resistance $\boldsymbol{R_m}$, is much harder and does not admit an analytical solution. Consequently, numerical methods have to be used. We first present the basic least-squares algorithm, and then describe four regularized least-squares algorithms with different regularization functions that aim to enhance the robustness of the reconstruction in the presence of measurement noises and modeling errors.

A. Least-Squares Minimization (LSM)

The inverse problem for the resistive network can be formulated as an optimization problem where the cost function to be minimized is the sum of squared residuals between the measured two-point resistances $\boldsymbol{R_m}$ and the calculated $\boldsymbol{R}$ based on Equation (10), with the requirement that the cell resistance is larger than or equal to the measured resistance:

$$\hat{\boldsymbol{r}} = \arg\min_{\boldsymbol{r}} \sum_{j=1,k=1}^{M,N} \left\| \boldsymbol{f}(\boldsymbol{r})_j^k - (\boldsymbol{R_m})_j^k \right\|^2 \tag{11}$$

$$\textbf{s.t. } \boldsymbol{r}_j^k \geq (\boldsymbol{R_m})_j^k \quad \text{for all } j \text{ and } k \tag{12}$$

where $\boldsymbol{r}_j^k$ is the cell resistance element at the pixel (j, k) while $(\boldsymbol{R_m})_j^k$ is the corresponding measured two-point resistance.

This least-squares problem is solved in MATLAB via the nonlinear least-square solver "lsqnonlin", which starts at an initial guess $\boldsymbol{r_0} \geq \boldsymbol{R_m}$ (where "$\geq$" holds true element-wise). The default algorithm for this solver is the trust-region-reflective algorithm based on the interior-reflective Newton method described in [60], which approximates the objective function by the first two terms of the Taylor-series approximation, restricts the trust-region subproblem to a two-dimensional subspace, and chooses the solver step to force global convergence via the gradient descent while achieving fast local convergence via the Newton step if it exists. The complete algorithm for this reconstruction method is given in Supporting Information Algorithm 2.

B. Least-Squares Regularization on Cell Resistance (LSR-CR)

The resistor network inverse problem suffers from its ill-posed nature; in particular, the numerical inverse solution depends sensitively on the input data and thus its performance is susceptible to measurement noises and modeling uncertainties. In order to reconstruct the cell resistance robustly and to give preference to particular solutions with desirable properties, the Tikhonov regularization technique is exploited, where a regularization term is included in the least squares minimization. One of the typical *a priori* regularization terms is the $\boldsymbol{L_2}$ regularization, $\lambda\|\boldsymbol{r}\|_2^2$, which is the sum of the squares of all elements from the inverse solution with a penalty weight

λ that penalizes large cell resistance values:

$$\hat{\boldsymbol{r}} = \arg\min_{\boldsymbol{r}} \sum_{j=1,k=1}^{M,N} \{ \left\| \boldsymbol{f}(\boldsymbol{r})_j^k - (\boldsymbol{R_m})_j^k \right\|^2 + \lambda \|\boldsymbol{r}_j^k\|^2 \} \quad (13)$$

$$\textbf{s.t. } \boldsymbol{r}_j^k \geq (\boldsymbol{R_m})_j^k \text{ for all } j \text{ and } k. \quad (14)$$

where $\lambda \geq 0$ is the regularization (or penalty) parameter, which determines the trade-off between the modeling discrepancy term and the regularization term. The regularization method in Equation (13) accommodates simultaneously the norm of the residual $[\boldsymbol{f}(\boldsymbol{r}) - \boldsymbol{R_m}]$ and the norm of the approximate solution $\boldsymbol{r}$, enforcing the *a priori* knowledge on solving the cell resistance, and improving the smoothness of the solution. The complete algorithm for this reconstruction method is given in Supporting Information Algorithm 3.

C. Least-Squares Regularization on Relative Change in Cell Resistance (LSR-ΔCR)

Different sensor pixels might have quite different cell resistances in the initial relaxed state before a pressure is applied, due to, for example, imperfect fabrication processes. So, an alternative regularization function would be the relative change in the cell resistance values, instead of these values themselves:

$$\begin{aligned}
&[\hat{\boldsymbol{r}}_0 \; \hat{\boldsymbol{r}}_1] \\
&= \arg\min_{\boldsymbol{r_0}\,\boldsymbol{r_1}} \sum_{j=1,k=1}^{M,N} \{ \left\| \boldsymbol{f}(\boldsymbol{r_0})_j^k - (\boldsymbol{R_{m0}})_j^k \right\|^2 \\
&\quad + \left\| \boldsymbol{f}(\boldsymbol{r_1})_j^k - (\boldsymbol{R_{m1}})_j^k \right\|^2 + \lambda \left\| \frac{(\boldsymbol{r_1})_j^k - (\boldsymbol{r_0})_j^k}{(\boldsymbol{r_0})_j^k} \times 100 \right\|^2 \} \quad (15)
\end{aligned}$$

$$\textbf{s.t. } (\boldsymbol{r_0})_j^k \geq (\boldsymbol{R_{m0}})_j^k \text{ and } (\boldsymbol{r_1})_j^k \geq (\boldsymbol{R_{m1}})_j^k \text{ for all } j \text{ and } k. \quad (16)$$

where $(\boldsymbol{r_0})_j^k$ and $(\boldsymbol{R_{m0}})_j^k$ are the cell resistance and the measured two-point resistance corresponding to the first group of measurements (e.g., prior to the application of the external pressure), while $(\boldsymbol{r_1})_j^k$ and $(\boldsymbol{R_{m1}})_j^k$ are those corresponding to the second group of measurements (e.g., after the pressure is applied). The data 100 in the equation denotes the percentage calculation in order to get the relative change in cell resistance.

The relative change in cell resistance is evaluated based on two consecutive cell resistance matrices. For the initialization step of this regularization, in order to calculate the relative change in cell resistance (in percentage), two groups of measured resistance $\boldsymbol{R_{m0}}$ and $\boldsymbol{R_{m1}}$ are required to be fed into Equation (15) at the beginning. Once the first two sets of cell resistance solutions $\boldsymbol{r_0}$ and $\boldsymbol{r_1}$ are solved jointly, $\boldsymbol{r_0}$, $\boldsymbol{R_{m0}}$, and $\boldsymbol{R_{m1}}$ are not used any more, while $\boldsymbol{r_1}$ is taken as the known new $\boldsymbol{r_0'}$. The next set of measured resistance $\boldsymbol{R_{m2}}$ will be used as the new $\boldsymbol{R_{m1}'}$, and Equation (15) will be replaced with a new regularization in order to find the corresponding solution $\boldsymbol{r_1'}$ for the new measurements:

$$\begin{aligned}
\hat{\boldsymbol{r}}_1' &= \arg\min_{\boldsymbol{r_1'}} \sum_{j=1,k=1}^{M,N} \{ \left\| \boldsymbol{f}(\boldsymbol{r_1'})_j^k - (\boldsymbol{R_{m1}'})_j^k \right\|^2 \\
&\quad + \lambda \left\| \frac{(\boldsymbol{r_1'})_j^k - (\boldsymbol{r_0'})_j^k}{(\boldsymbol{r_0'})_j^k} \times 100 \right\|^2 \} \quad (17)
\end{aligned}$$

$$\textbf{s.t. } (\boldsymbol{r_1'})_j^k \geq (\boldsymbol{R_{m1}'})_j^k \text{ for all } j \text{ and } k. \quad (18)$$

The reconstruction will be initialized first and then be updated iteratively for the following steps. The complete algorithm for this method is given in Supporting Information Algorithm 4.

D. Least-Squares Regularization on Gradient of Cell Resistance (LSR-∇CR)

We also consider using the cell resistance gradient as the regularization term to minimize spikes in the mapping contours. This method is captured as below:

$$\hat{\boldsymbol{r}} = \arg\min_{\boldsymbol{r}} \sum_{j=1,k=1}^{M,N} \{ \left\| \boldsymbol{f}(\boldsymbol{r})_j^k - (\boldsymbol{R_m})_j^k \right\|^2 + \lambda \|\nabla \boldsymbol{r}_j^k\|^2 \} \quad (19)$$

$$\textbf{s.t. } \boldsymbol{r}_j^k \geq (\boldsymbol{R_m})_j^k \text{ for all } j \text{ and } k. \quad (20)$$

The complete algorithm for this reconstruction method is given in Supporting Information Algorithm 5.

The gradient can be calculated differently according to the location of the pixel. If the pixel is in the interior of the sensing matrix, the gradient components are approximated by the central difference between the neighboring pixels. If the pixel is on the boundary, the appropriate gradient components are calculated with single-sided differences. The gradient calculation steps are summarized in Supporting Information Algorithm 6.

E. Least-Squares Regularization on Gradient of Relative Change in Cell Resistance (LSR-$\nabla\Delta$CR)

Finally, we consider regularization based on the gradient of the relative change in cell resistance

$$\begin{aligned}
&[\hat{\boldsymbol{r}}_0 \; \hat{\boldsymbol{r}}_1] \\
&= \arg\min_{\boldsymbol{r_0}\,\boldsymbol{r_1}} \sum_{j=1,k=1}^{M,N} \{ \left\| \boldsymbol{f}(\boldsymbol{r_0})_j^k - (\boldsymbol{R_{m0}})_j^k \right\|^2 \\
&\quad + \left\| \boldsymbol{f}(\boldsymbol{r_1})_j^k - (\boldsymbol{R_{m1}})_j^k \right\|^2 \\
&\quad + \lambda \left\| \nabla \left(\frac{(\boldsymbol{r_1})_j^k - (\boldsymbol{r_0})_j^k}{(\boldsymbol{r_0})_j^k} \times 100 \right) \right\|^2 \} \quad (21)
\end{aligned}$$

$$\textbf{s.t. } (\boldsymbol{r_0})_j^k \geq (\boldsymbol{R_{m0}})_j^k \text{ and } (\boldsymbol{r_1})_j^k \geq (\boldsymbol{R_{m1}})_j^k \text{ for all } j \text{ and } k. \quad (22)$$

where two consecutive sets of measured resistances $\boldsymbol{R_{m0}}$ and $\boldsymbol{R_{m1}}$ are required for initialization at the beginning, and the gradient of the relative change in cell resistance can be calculated accordingly. The updating rule of this algorithm is similar to that in the reconstruction method LSR-ΔCR: first, solve $\boldsymbol{r_0}$ and $\boldsymbol{r_1}$ jointly; then, take $\boldsymbol{r_1}$ as the known new $\boldsymbol{r_0'}$; and next, take a third set of resistance measurement as the new $\boldsymbol{R_{m1}'}$, and the corresponding new cell resistance $\boldsymbol{r_1'}$ could be generated from the following regularization:

$$\hat{\boldsymbol{r}}_1' = \arg\min_{\boldsymbol{r_1'}} \sum_{j=1,k=1}^{M,N} \{ \left\| \boldsymbol{f}(\boldsymbol{r_1'})_j^k - (\boldsymbol{R_{m1}'})_j^k \right\|^2$$

$$+ \lambda \left\| \nabla \left(\frac{(\boldsymbol{r}_1')_j^k - (\boldsymbol{r}_0')_j^k}{(\boldsymbol{r}_0')_j^k} \times 100 \right) \right\|^2 \} \tag{23}$$

$$\textbf{s.t. } (\boldsymbol{r}_1')_j^k \geq (\boldsymbol{R}_{m1}')_j^k \text{ for all } j \text{ and } k. \tag{24}$$

The reconstruction will be updated iteratively with the new measurements coming in, using the latest measurement as (R_{m1}) and using the previous solution as $\boldsymbol{r_0}$ in order to guarantee the solving process to be consecutive and consistent. The complete algorithm is given in Supporting Information Algorithm 7, which is similar with Algorithm 4 with both the initialization step and the following steps, the only difference is that the regularization terms are now the gradient of the relative change in cell resistance.

V. Experiments

A. Experimental Animals

In August 2020, thirty spawning phase adult sea lampreys were tested on the 10-by-10 pressure sensing panel. These sea lampreys were captured in traps during upstream spawning migration in the St. Marys River (Michigan, USA and Ontario, Canada) during May-July 2020. Traps were operated by Canada Department of Fisheries and Oceans and the U. S. Fish and Wildlife Service.

Lampreys were transported to the U. S. Geological Survey Great Lakes Science Center's Hammond Bay Biological Station, Millersburg, Michigan, USA where they were held in aerated 1000 L tanks supplied continuously with Lake Huron water (salinity: 0 ppt, pH: 7-8) maintained at 8-12 °C with a dissolved oxygen saturation of over 90 % in the sea lampreys until tests were conducted. Prior to tests, body weight, total body length, and mouth diameter were measured (see Table TI in Supporting Information). All sea lamprey experiments were performed in accordance with protocols and guidelines approved by Michigan State University's Institutional Animal Care and Use Committee (IACUC, No. 02/18-028-00). After the suction pressure experiments in this study, the sea lampreys were housed for use in further research by Hammond Bay Biological Station staff.

B. Experimental Setup

As shown in Fig. 7, the resistance of the pressure sensors at each pixel was measured by a voltage divider with a 1k ohm reference resistor. An Arduino Mega 2560 microcontroller board provided a 5 V voltage supply for the pressure sensing circuits, and generated digital output signals for channel selection. Two analog/digital multiplexer breakout boards (SparkFun CD74HC4067, 16 channels) were used to choose the circuits between one column and one row of the perpendicular address lines. The output voltage on the reference resistor could be measured by a 10-bit Analog-to-Digital Converter (ADC) through the analog input.

The experimental setup is shown in Fig. 7-a, in the experimental water tank (200 L). The pressure sensing panel was placed vertically on the acrylic hanger along a glass wall of the water tank, while the Arduino Mega board and the voltage divider on the breadboard were adhered on the other side of the hanger. The acrylic hanger was clamped on the water tank wall via two clamps. The water level in the tank was about 5 cm higher than the top row electrode of the 10-by-10 pressure sensing panel, submerging all the sensing area.

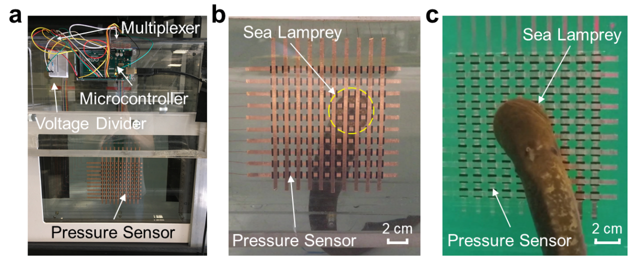

Fig. 7. Experimental setup of the pressure sensing system for sea lamprey detection.(a) The pressure sensing panel and the hardware attached on the back side of the panel, (b) the back view of the pressure sensing panel with an adult sea lamprey attaching on it, and (c) the front view of the pressure sensing panel with another adult sea lamprey attaching on it.

C. Experiment on Sea Lampreys With the Pressure Sensor

In each round of measurement, the pressure sensing system scanned the pressure sensors from the top left corner (X = 1, Y = 1) to the bottom right corner (X = 10, Y = 10) by selecting the channels of the multiplexers. Resistance was measured consecutively for 20 times at each pressure sensor, and then the average was taken as the measured two-point resistance at that pixel for that time instance. The Arduino program would repeat the scanning and measurement process every one second (overall sampling rate: 1 Hz) in loops by means of timer interrupt. The resistance measurement data would be stored in the computer hard drive once the program was closed.

Once the Arduino program started to run and measure the resistance periodically, an adult sea lamprey was transferred to the tank and allowed to explore the tank until it attached to the tank surface via oral suction. If the lamprey did not attach onto the sensing area, it would be gently repositioned and held with its mouth over the sensing area until it attached. The top surface of the sensing area was relatively smooth, and experiments showed that most of the tested sea lampreys were able to attach to this sensor for a certain time (e.g., $>$ 20 s) after a few trials. As demonstrated in Fig. 7-b, c, a sea lamprey was attached onto the central area of the sensing panel, with a region spanning almost 4 rows and 4 columns of copper tapes covered by the sea lamprey's oral disc. Resistance measurement lasted until the lamprey volitionally detached from the panel or until the first 2 minutes of attachment elapsed. The measurement data would be processed to plot the mapping contours of relative change in the measured resistance directly, or would be used to reconstruct the cell resistance first using one of the reconstruction methods proposed in Section IV, and then to plot the mapping contours of the relative change in cell resistance.

VI. Results

A. Comparison Between Different Methods

To have a better understanding of all the methods explored above, mapping contours from these methods are displayed

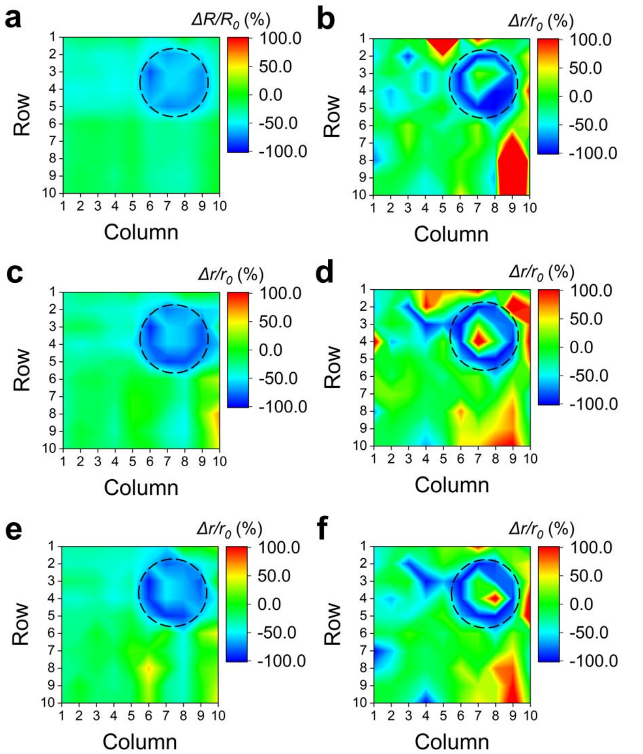

Fig. 8. Comparison between mapping contours from different methods. Mapping contours of (a) relative change in directly measured two-point resistance, (b) relative change in cell resistance from least-squares minimization (LSM), (c) relative change in cell resistance from least-squares regularization on the cell resistance (LSR-CR) with $\lambda = 0.001$, (d) relative change in cell resistance from least-squares regularization on the relative change in cell resistance (LSR-ΔCR) with $\lambda = 10$, (e) relative change in cell resistance from least-squares regularization on the gradient of cell resistance (LSR-∇CR) with $\lambda = 0.001$, and (f) relative change in cell resistance from least-squares regularization on the gradient of relative change in cell resistance (LSR-$\nabla\Delta$R) with $\lambda = 10$.

in the same panel in Fig. 8. For each regularization method, a mapping contour with "best" choice of λ is selected (by "best", we mean visually perceived best tradeoff between data matching and smoothing). Fig. 8-a shows the mapping contour of the relative change in the measured resistance (between -82.6% and -1.8%), which is a baseline for all the other results. Fig. 8-b is the result from least-squares minimization (LSM algorithm without regularization) with the relative change in cell resistance between -99.5% and 11873.9%, and the following four mapping contours are the results of relative change in cell resistance based on regularization on the cell resistance (LSR-CR algorithm, Fig. 8-c, $\lambda = 0.001$, between -94% and 71%), regularization on the relative change in cell resistance (LSR-ΔCR algorithm, Fig. 8-d, $\lambda = 10$, between -99.9% and 185%), regularization on the gradient of cell resistance (LSR-∇CR algorithm, Fig. 8-e, $\lambda = 0.001$, between -97% and 59%), and lastly regularization on the gradient of relative change in cell resistance (LSR-$\nabla\Delta$CR algorithm, Fig. 8-f, $\lambda = 10$, between -99.9% and 155%), respectively.

As observed above, with the same color bar range, (1) directly measured resistance change (Fig. 8-a) is "blurry" as the measured resistance is related to the cell resistance through a nonlinear filter. (2) Plain LSM (Fig. 8-b) produces large spikes at some pixels outside of the actual suction area, since this reconstruction method is susceptible to the effect of measurement noises and modeling errors. (3) LSR-CR (Fig. 8-c) and LSR-∇CR (Fig. 8-e) produce more distinct patterns than directly measured resistance changes while showing pronounced smoothing effect. And (4) LSR-ΔCR (Fig. 8-d) and LSR-$\nabla\Delta$CR (Fig. 8-f) produce the most distinct suction patterns with cell resistance decreased along the rim of the oral disc and with cell resistance increased within oral disc.

TABLE I
PERFORMANCE COMPARISON OF DIFFERENT METHODS

Method	Specifications	Computation Time [s]	Absolute Relative Error [%]
LSM	Least Squares Minimization	16.45 ± 0.40	1.33 ± 1.29
LSR-CR	Regularization on Cell Resistance	10.20 ± 2.04	7.36 ± 7.85
LSR-ΔCR	Regularization on Relative Change in Cell Resistance	58.63	1.19 ± 1.18
	Following Steps after Initialization	8.05 ± 0.88	1.48 ± 1.51
LSR-∇CR	Regularization on Gradient of Cell Resistance	11.46 ± 1.71	5.67 ± 5.28
LSR-$\Delta\nabla$CR	Regularization on Gradient of Relative Change in Cell Resistance	60.85	1.13 ± 1.13
	Following Steps after Initialization	11.01 ± 0.96	1.48 ± 1.48

Data are presented in the type of mean ± standard deviation.

In order to further compare the performance of different reconstruction methods, 21 consecutive sets of measured 10-by-10 two-point resistance matrices obtained during the sea lamprey test were used for running these algorithms in MATLAB R2020b on the laptop with a CPU of Intel i7-6700HQ (2.60 GHz) and a 16.0 GB RAM. The computation time and absolute relative error (in percentage) between the derived two-point resistance and the measured two-point resistance were calculated in the form of "mean $\pm$ standard deviation" and are listed in Table I.

For the regularization methods LSR-ΔCR and LSR-$\nabla\Delta$CR, the initialization step took 58.63 s and 60.85 s, respectively, while the following steps took only 8.05 ± 0.88 s and 11.01 ± 0.96. The reason for significantly longer computation time in the initialization step is because these two methods need to solve for both matrices $\boldsymbol{r_0}$ and $\boldsymbol{r_1}$ jointly. But for the steps after, the computation time dropped greatly while the absolute relative errors remained within a desirable range. On the other hand, the computation time for the method LSM was 16.45 ± 0.40 s, which was larger than the other methods like LSR-CR and LSR-∇CR. Although it had a smaller absolute relative error, the mapping contour did not reflect a perfect visualization result given the noise and the displayed shape. The final decision of reconstruction methods will be a trade-off between the computational complexity, the relative error in data matching, and the smoothing effect. Note that the mapping contours of relative change in measured two-point resistance could still be used instantaneously in real-time lamprey attachment detection, which takes about 0.31 s computation time to plot the mapping contour for each round of new measurements in MATLAB using the $surf(\cdot)$ function. The reconstruction methods require some time to compute the

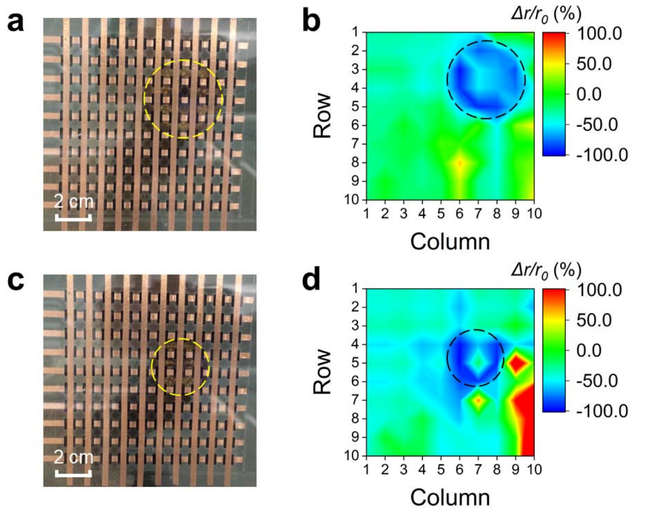

Fig. 9. Comparison of the mapping contours between sea lampreys with large and small mouth diameters. (a) An adult sea lamprey attaching on the sensing panel with a mouth diameter of about 35 mm, and (b) the mapping contour corresponding to the attachment condition in (a) using the LSR-∇CR method. (c) Another smaller adult sea lamprey attaching on the sensing panel with a mouth diameter of about 25 mm, and (d) the mapping contour corresponding to the attachment condition in (c) using the LSR-∇CR method.

cell resistance change and will be best for post-processing to gain further information about the detected animal.

B. Mapping Contour Comparison Between Sea Lampreys With Large and Small Mouth Diameters

For demonstration, the least-squares regularization method on the gradient of cell resistance (LSR-∇CR) with $\lambda = 0.001$ is chosen to further show the capability of the proposed sensor panel in capturing the demographic information of the detected lampreys. The mapping contours of the 10-by-10 pressure sensing panel under suction and attachment of two different adult sea lampreys are shown in Fig. 9. The first adult male sea lamprey had a mouth diameter of 35 mm (as shown in Supporting Video 1), while the other adult male had a mouth diameter of 25 mm (as shown in Supporting Video 2). From the figures, we can observe that the blue mapping contour for the larger mouth was covering a 4-by-4 grid area (6a-b), while the smaller one was covering a 3-by-3 grid area (6c-d), indicating the ability to successfully measure the size of the sea lamprey's mouth attaching on the sensing panel.

VII. Conclusion and Future Work

An effective sensing technique to autonomously detect and monitor sea lampreys will be of significant interest to the sea lamprey control effort in the Great Lakes and potentially to programs that seek to conserve or restore lampreys elsewhere throughout their native ranges. Motivated by this practical application, we developed a low-cost and efficient piezoresistive pressure sensor based on a passive resistor network and proposed new algorithms for properly processing the measured data to reconstruct the pressure pattern. In particular, in order to recover the cell resistance from the measured two-point resistance, we derived the general inverse mapping relationship based on basic Kirchhoff's current law, and introduced several inverse algorithms based on the least-squares minimization and Tikhonov regularization. These approaches are novel and distinct from previous reports as our methods are general and applicable to a passive resistor network of any size, with the measurement noises and modelling uncertainties taken into consideration. The approaches were validated with results from experiments with live sea lampreys. The pros and cons of the different reconstruction methods were discussed in depth. While the sensing system was motivated by the sea lamprey detection problem, it is applicable to other applications in soft robotics, wearable electronics, biomonitoring, and human-machine interfaces.

The choice of the value of the regularization parameter λ in this paper was determined by trying a few values in different orders of magnitude. While more principled methods of choosing the λ value are available in the literature, such as the Morozov discrepancy principle [54], and the ordinary cross-validation criteria [55], these methods are mostly applicable for linear models. Developing a more systematic approach to choosing the regularization parameter remains a direction for our future work. In addition, we will explore the refinement of the fabrication methods to improve both spatial resolution and scalability. Scalability is important for practical deployment of the sensing panel in detecting sea lampreys in fish passages or other natural environments. For that purpose, we will investigate approaches to integration of modular, elementary panels into larger panels (up to the size of 1 m × 1 m). We will also examine data analytics algorithms for automated recognition of suction patterns (instead of relying on human recognition).

Finally, the developed pressure sensor is encapsulated and waterproofed; as such, environmental factors such as the pH value, oxygen saturation, and conductivity of the water are not expected to affect the outputs of the sensor. However, some other factors, such as the water temperature and the depth-induced hydrostatic pressure could have an impact on the sensor outputs. We will conduct further animal experiments to characterize the potential dependence of the sensor outputs on water temperatures and sensor deployment depths, and if needed, we will develop corresponding compensation algorithms to counter the influence of these environmental variables.

Acknowledgment

The authors thank Mohammed Al-Rubaiai for his discussion in the exploration of Velostat films, Jacob Blatt for his help in the initial test of the pressure sensors, Xinda Qi for his discussion in the resistor network, and Trisha Searcy for her great assistance in the lamprey tests. Any use of trade, product, or firm names is for descriptive purposes only and does not imply endorsement by the U.S. Government.

References

[1] J. E. Marsden and M. J. Siefkes, "Control of invasive sea lamprey in the Great Lakes, Lake Champlain, and Finger Lakes of New York," in *Lampreys: Biology, Conservation and Control*, vol. 2, J. Margaret and F. Docker, Eds. Corvallis, OR, USA: McGraw-Hill, 2019, pp. 411–479.

[2] W. D. Swink, "Host selection and lethality of attacks by sea lampreys (*Petromyzon marinus*) in laboratory studies," *J. Great Lakes Res.*, vol. 29, pp. 307–319, Jan. 2003.

[3] N. S. Johnson, H. T. Thompson, C. Holbrook, and J. A. Tix, "Blocking and guiding adult sea lamprey with pulsed direct current from vertical electrodes," *Fisheries Res.*, vol. 150, pp. 38–48, Feb. 2014.

[4] R. L. McLaughlin, A. Hallett, T. C. Pratt, L. M. O'Connor, and D. G. McDonald, "Research to guide use of barriers, traps, and fishways to control sea lamprey," *J. Great Lakes Res.*, vol. 33, no. sp2, pp. 7–19, Sep. 2007.

[5] T. C. Pratt *et al.*, "Balancing aquatic habitat fragmentation and control of invasive species: Enhancing selective fish passage at sea lamprey control barriers," *Trans. Amer. Fisheries Soc.*, vol. 138, no. 3, pp. 652–665, 2009.

[6] H. R. Dodd *et al.*, "Low-head sea lamprey barrier effects on stream habitat and fish communities in the Great Lakes Basin," *J. Great Lakes Res.*, vol. 29, pp. 386–402, Jan. 2003.

[7] R. L. McLaughlin *et al.*, "Unintended consequences and trade-offs of fish passage," *Fish Fisheries*, vol. 14, no. 4, pp. 580–604, Dec. 2013.

[8] C. Negrea, D. E. Thompson, S. D. Juhnke, D. S. Fryer, and F. J. Loge, "Automated detection and tracking of adult Pacific lampreys in underwater video collected at snake and Columbia river fishways," *North Amer. J. Fisheries Manage.*, vol. 34, no. 1, pp. 111–118, Feb. 2014.

[9] Á. Rodríguez, M. Bermúdez, J. R. Rabuñal, and J. Puertas, "Fish tracking in vertical slot fishways using computer vision techniques," *J. Hydroinform.*, vol. 17, no. 2, pp. 275–292, Mar. 2015.

[10] I. C. Potter, H. S. Gill, C. B. Renaud, and D. Haoucher, "The taxonomy, phylogeny, and distribution of lampreys," in *Lampreys: Biology, Conservation and Control*, vol. 1, J. Margaret and F. Docker, Eds. Corvallis, OR, USA: McGraw-Hill, 2015, pp. 35–73.

[11] R. D. Adams, "Suction pressure measurement and behavioral observations of spawning-run sea lampreys (*Petromyzon marinus*)," M.S. thesis, Dept. Biol., Eastern Michigan Univ., Ypsilanti, MI, USA, 2006.

[12] H. Shi, C. M. Holbrook, Y. Cao, N. Sepúlveda, and X. Tan, "Measurement of suction pressure dynamics of sea lampreys, *Petromyzon marinus*," *PLoS ONE*, vol. 16, no. 4, Apr. 2021, Art. no. e0247884.

[13] I. González-Afanador, H. Shi, C. Holbrook, X. Tan, and N. Sepulveda, "Invasive sea lamprey detection and characterization using interdigitated electrode (IDE) contact sensor," *IEEE Sensors J.*, vol. 21, no. 24, pp. 27947–27956, Dec. 2021.

[14] H. Park *et al.*, "Stretchable array of highly sensitive pressure sensors consisting of polyaniline nanofibers and Au-coated polydimethylsiloxane micropillars," *ACS Nano*, vol. 9, no. 10, pp. 9974–9985, Oct. 2015.

[15] R. Matsuda *et al.*, "Highly stretchable sensing array for independent detection of pressure and strain exploiting structural and resistive control," *Sci. Rep.*, vol. 10, no. 1, p. 12666, Dec. 2020.

[16] S. Cheng, Y. S. Narang, C. Yang, Z. Suo, and R. D. Howe, "Stick-on large-strain sensors for soft robots," *Adv. Mater. Interfaces*, vol. 6, no. 20, Oct. 2019, Art. no. 1900985.

[17] S. Zhang *et al.*, "Fully printed silver-nanoparticle-based strain gauges with record high sensitivity," *Adv. Electron. Mater.*, vol. 3, no. 7, Jul. 2017, Art. no. 1700067.

[18] A. M. Soomro, M. A. U. Khalid, I. Shah, S. W. Kim, Y. S. Kim, and K. H. Choi, "Highly stable soft strain sensor based on Gly-KCl filled sinusoidal fluidic channel for wearable and water-proof robotic applications," *Smart Mater. Struct.*, vol. 29, no. 2, Feb. 2020, Art. no. 025011.

[19] A. Chhetry, S. Sharma, H. Yoon, S. Ko, and J. Y. Park, "Enhanced sensitivity of capacitive pressure and strain sensor based on $CaCu_3Ti_4O_{12}$ wrapped hybrid sponge for wearable applications," *Adv. Funct. Mater.*, vol. 30, no. 31, Aug. 2020, Art. no. 1910020.

[20] M. Fu, J. Zhang, Y. Jin, Y. Zhao, S. Huang, and C. F. Guo, "A highly sensitive, reliable, and high-temperature-resistant flexible pressure sensor based on ceramic nanofibers," *Adv. Sci.*, vol. 7, no. 17, Sep. 2020, Art. no. 2000258.

[21] Y. Zhang *et al.*, "Highly stretchable and sensitive pressure sensor array based on icicle-shaped liquid metal film electrodes," *ACS Appl. Mater. Interfaces*, vol. 12, no. 25, pp. 27961–27970, 2020.

[22] W. Asghar *et al.*, "Piezocapacitive flexible e-skin pressure sensors having magnetically grown microstructures," *Adv. Mater. Technol.*, vol. 5, no. 2, Feb. 2020, Art. no. 1900934.

[23] S. R. A. Ruth, L. Beker, H. Tran, V. R. Feig, N. Matsuhisa, and Z. Bao, "Rational design of capacitive pressure sensors based on pyramidal microstructures for specialized monitoring of biosignals," *Adv. Funct. Mater.*, vol. 30, no. 29, Jul. 2020, Art. no. 1903100.

[24] X. Hou *et al.*, "Flexible piezoelectric nanofibers/polydimethylsiloxane-based pressure sensor for self-powered human motion monitoring," *Energy Technol.*, vol. 8, no. 3, Mar. 2020, Art. no. 1901242.

[25] Y. Su *et al.*, "Muscle fibers inspired high-performance piezoelectric textiles for wearable physiological monitoring," *Adv. Funct. Mater.*, vol. 31, no. 19, 2021, Art. no. 2010962.

[26] W. Lin, B. Wang, G. Peng, Y. Shan, H. Hu, and Z. Yang, "Skin-inspired piezoelectric tactile sensor array with crosstalk-free row+column electrodes for spatiotemporally distinguishing diverse stimuli," *Adv. Sci.*, vol. 8, no. 3, Feb. 2021, Art. no. 2002817.

[27] Y. Cao, J. Figueroa, W. Li, Z. Chen, Z. L. Wang, and N. Sepúlveda, "Understanding the dynamic response in ferroelectret nanogenerators to enable self-powered tactile systems and human-controlled micro-robots," *Nano Energy*, vol. 63, Sep. 2019, Art. no. 103852.

[28] Y. Cao, W. Li, and N. Sepúlveda, "Performance of self-powered, water-resistant bending sensor using transverse piezoelectric effect of polypropylene ferroelectret polymer," *IEEE Sensors J.*, vol. 19, no. 22, pp. 10327–10335, Nov. 2019.

[29] Y. Cao and N. Sepúlveda, "Design of flexible piezoelectric gyroscope for structural health monitoring," *Appl. Phys. Lett.*, vol. 115, no. 24, Dec. 2019, Art. no. 241901.

[30] L. Gao *et al.*, "All paper-based flexible and wearable piezoresistive pressure sensor," *ACS Appl. Mater. Interfaces*, vol. 11, no. 28, pp. 25034–25042, Jul. 2019.

[31] T. Zhao, T. Li, L. Chen, L. Yuan, X. Li, and J. Zhang, "Highly sensitive flexible piezoresistive pressure sensor developed using biomimetically textured porous materials," *ACS Appl. Mater. Interfaces*, vol. 11, no. 32, pp. 29466–29473, Aug. 2019.

[32] C.-L. Choong *et al.*, "Highly stretchable resistive pressure sensors using a conductive elastomeric composite on a micropyramid array," *Adv. Mater.*, vol. 26, no. 21, pp. 3451–3458, 2014.

[33] M. Ntagios, H. Nassar, A. Pullanchiyodan, W. T. Navaraj, and R. Dahiya, "Robotic hands with intrinsic tactile sensing via 3D printed soft pressure sensors," *Adv. Intell. Syst.*, vol. 2, no. 6, Jun. 2020, Art. no. 1900080.

[34] H. A. Sonar, A. P. Gerratt, S. P. Lacour, and J. Paik, "Closed-loop haptic feedback control using a self-sensing soft pneumatic actuator skin," *Soft Robot.*, vol. 7, no. 1, pp. 22–29, Feb. 2020.

[35] T. Sekine *et al.*, "Microporous induced fully printed pressure sensor for wearable soft robotics machine interfaces," *Adv. Intell. Syst.*, vol. 2, no. 12, Dec. 2020, Art. no. 2000179.

[36] N. Bai *et al.*, "Graded intrafillable architecture-based iontronic pressure sensor with ultra-broad-range high sensitivity," *Nature Commun.*, vol. 11, no. 1, p. 209, Dec. 2020.

[37] H. Shi *et al.*, "Screen-printed soft capacitive sensors for spatial mapping of both positive and negative pressures," *Adv. Funct. Mater.*, vol. 29, no. 23, 2019, Art. no. 1809116.

[38] L. An *et al.*, "Soft sensor for measuring wind pressure," *Int. J. Mech. Sci.*, vol. 141, pp. 386–392, Jun. 2018.

[39] L. Lo, H. Shi, H. Wan, Z. Xu, X. Tan, and C. Wang, "Inkjet-printed soft resistive pressure sensor patch for wearable electronics applications," *Adv. Mater. Technol.*, vol. 5, no. 1, Jan. 2020, Art. no. 1900717.

[40] S. R. A. Ruth, V. R. Feig, M.-G. Kim, Y. Khan, J. K. Phong, and Z. Bao, "Flexible fringe effect capacitive sensors with simultaneous high-performance contact and non-contact sensing capabilities," *Small Struct.*, vol. 2, no. 2, Feb. 2021, Art. no. 2000079.

[41] D. Yoo, D. Won, W. Cho, J. Lim, and J. Kim, "Double side electromagnetic interference-shielded bending-insensitive capacitive-type flexible touch sensor with linear response over a wide detection range," *Adv. Mater. Technol.*, vol. 6, no. 11, Nov. 2021, Art. no. 2100358.

[42] E. Jeong, J. Lee, and D. Kim, "Finger-gesture recognition glove using Velostat (ICCAS 2011)," in *Proc. 11th Int. Conf. Control, Autom. Syst.*, Gyeonggi-do, South Korea, 2011, pp. 206–210.

[43] S. Sundaram, P. Kellnhofer, Y. Li, J.-Y. Zhu, A. Torralba, and W. Matusik, "Learning the signatures of the human grasp using a scalable tactile glove," *Nature*, vol. 569, no. 7758, pp. 698–702, 2019.

[44] J. Tolvanen, J. Hannu, and H. Jantunen, "Hybrid foam pressure sensor utilizing piezoresistive and capacitive sensing mechanisms," *IEEE Sensors J.*, vol. 17, no. 15, pp. 4735–4746, Aug. 2017.

[45] B. W. Lee and H. Shin, "Feasibility study of sitting posture monitoring based on piezoresistive conductive film-based flexible force sensor," *IEEE Sensors J.*, vol. 16, no. 1, pp. 15–16, Jan. 2016.

[46] M. Hopkins, R. Vaidyanathan, and A. H. Mcgregor, "Examination of the performance characteristics of Velostat as an in-socket pressure sensor," *IEEE Sensors J.*, vol. 20, no. 13, pp. 6992–7000, Jul. 2020.

[47] D. Giovanelli and E. Farella, "Force sensing resistor and evaluation of technology for wearable body pressure sensing," *J. Sensors*, vol. 2016, Feb. 2016, Art. no. 9391850.

[48] S. S. Suprapto, A. W. Setiawan, H. Zakaria, W. Adiprawita, and B. Supartono, "Low-cost pressure sensor matrix using Velostat," in *Proc. 5th Int. Conf. Instrum., Commun., Inf. Technol., Biomed. Eng. (ICICI-BME)*, Bandung, Indonesia, Nov. 2017, pp. 137–140.

[49] F. Y. Wu, "Theory of resistor networks: The two-point resistance," *J. Phys. A, Math. Gen.*, vol. 37, no. 26, pp. 6653–6673, Jul. 2004.

[50] N. S. Izmailian, R. Kenna, and F. Y. Wu, "The two-point resistance of a resistor network: A new formulation and application to the cob-web network," *J. Phys. A, Math. Theory*, vol. 47, no. 3, Dec. 2014, Art. no. 035003.

[51] R. S. Saxena, N. K. Saini, and R. K. Bhan, "Analysis of crosstalk in networked arrays of resistive sensors," *IEEE Sensors J.*, vol. 11, no. 4, pp. 920–924, Apr. 2011.

[52] J. Wu, L. Wang, and J. Li, "Design and crosstalk error analysis of the circuit for the 2-D networked resistive sensor array," *IEEE Sensors J.*, vol. 15, no. 2, pp. 1020–1026, Feb. 2015.

[53] C. Medrano-Sánchez, R. Igual-Catalán, V. H. Rodríguez-Ontiveros, and I. Plaza-García, "Circuit analysis of matrix-like resistor networks for eliminating crosstalk in pressure sensitive mats," *IEEE Sensors J.*, vol. 19, no. 18, pp. 8027–8036, Sep. 2019.

[54] J. Kaipio and E. Somersalo, *Statistical and Computational Inverse Problems*. New York, NY, USA: Springer, 2006.

[55] C. Cohen-Bacrie, Y. Goussard, and R. Guardo, "Regularized reconstruction in electrical impedance tomography using a variance uniformization constraint," *IEEE Trans. Med. Imag.*, vol. 16, no. 5, pp. 562–571, Oct. 1997.

[56] K. Takei *et al.*, "Nanowire active-matrix circuitry for low-voltage macroscale artificial skin," *Nature Mater.*, vol. 9, no. 10, pp. 821–826, 2010.

[57] C. Wang *et al.*, "User-interactive electronic skin for instantaneous pressure visualization," *Nature Mater.*, vol. 12, pp. 899–904, Jul. 2013.

[58] C. Yeom, K. Chen, D. Kiriya, Z. Yu, G. Cho, and A. Javey, "Large-area compliant tactile sensors using printed carbon nanotube active-matrix backplanes," *Adv. Mater.*, vol. 27, no. 9, pp. 1561–1566, 2015.

[59] M. Gehre *et al.*, "Sparsity reconstruction in electrical impedance tomography: An experimental evaluation," *J. Comput. Appl. Math.*, vol. 236, no. 8, pp. 2126–2136, Feb. 2012.

[60] T. F. Coleman and Y. Li, "An interior, trust region approach for nonlinear minimization subject to bounds," *SIAM J. Optim.*, vol. 6, no. 2, pp. 418–445, 1996.

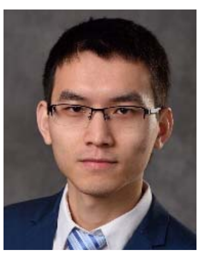

Hongyang Shi (Graduate Student Member, IEEE) received the B.S. degree in mechanical design, manufacturing and automation and the M.S. degree in mechatronics engineering from the Huazhong University of Science and Technology (HUST), Wuhan, China, in 2012 and 2015, respectively. He is currently pursuing the Ph.D. degree in electrical and computer engineering with Michigan State University (MSU), MI, USA.

He was a Mechanical Engineer with INMOTION Technologies, Shenzhen, China, before studying as a Ph.D. Student at MSU in Fall 2016. His research interests include soft robotics and electronic sensors. He was a recipient of the China National Scholarship (2010), the China National Endeavor Fellowship (2011), the FESTO Scholarship (2012) from HUST, the MSU Engineering Distinguished Fellowship (2016), the Graduate Office Fellowship (2018), the Dissertation Completion Fellowship (2021), and the Fitch H. Beach Award (2022) from the College of Engineering at MSU.

Ian González-Afanador (Student Member, IEEE) received the B.S. degree in electrical and computer engineering from the University of Puerto Rico, Mayagüez, Puerto Rico, in 2019. He is currently pursuing the Ph.D. degree in electrical and computer engineering with Michigan State University.

He has had internships with Honeywell Aerospace and Lockheed-Martin Sikorsky. He has participated in summer research programs at the University of Virginia, Michigan State University, and Georgia Tech. His current research focuses on the development of underwater biological contact/accumulation and development of piezoelectric-based anti-fouling systems for light sources used in algal cultivation.

Mr. Gonzalez-Afanador was a recipient of the NSF Graduate Research Fellowship and the MSU University Distinguished Fellowship.

Christopher Holbrook received the bachelor's and Master of Science degrees in zoology from The University of Maine, USA, and the Doctor of Philosophy degree in fisheries and wildlife from Michigan State University, USA. His research focuses on fish ecology and fisheries management.

Nelson Sepúlveda (Senior Member, IEEE) received the B.S. degree in electrical and computer engineering from the University of Puerto Rico, Mayagüez, Puerto Rico, in 2001, and the M.S. and Ph.D. degrees in electrical and computer engineering from Michigan State University (MSU), East Lansing, MI, USA, in 2002 and 2005, respectively. During the last year of graduate school, he attended the Sandia National Laboratories. In 2006, he joined as a Faculty Member at the Department of Electrical and Computer Engineering, University of Puerto Rico. He was a Visiting Faculty Researcher at the Air Force Research Laboratories (2006, 2007, 2013, and 2014), the National Nanotechnology Infrastructure Network (2008), and the Cornell Center for Materials Research (2009); the last two being the National Science Foundation (NSF) funded centers at Cornell University, Ithaca, NY, USA. In 2011, he joined as a Faculty Member at the Department of Electrical and Computer Engineering, MSU, where he is currently a Professor. His current research interests include smart materials and the integration of such in microelectromechanical systems, with particular emphasis on vanadium dioxide thin films and the use of the structural phase transition for the development of smart microactuators. He has received the NSF CAREER Award in 2010 and the MSU Teacher Scholar Award in 2015.

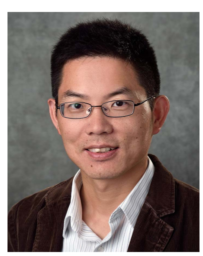

Xiaobo Tan (Fellow, IEEE) received the B.Eng. and M.Eng. degrees in automatic control from Tsinghua University, Beijing, China, in 1995 and 1998, respectively, and the Ph.D. degree in electrical and computer engineering from the University of Maryland, College Park, in 2002.

He is currently an MSU Foundation Professor and the Richard M. Hong Endowed Chair in Electrical and Computer Engineering at Michigan State University (MSU). His research interests include modeling and control of systems with hysteresis, electroactive polymer sensors and actuators, soft robotics, and bio-inspired underwater robots and their application to environmental sensing. He has published over 300 papers and been awarded four U.S. patents in these areas. He is a Fellow of ASME. He was a recipient of the NSF CAREER Award (2006), the MSU Teacher-Scholar Award (2010), the MSU College of Engineering Withrow Distinguished Scholar Award (2018), the Distinguished Alumni Award from the Department of Electrical and Computer Engineering at University of Maryland (2018), and multiple best paper awards. He serves as a Senior Editor for IEEE/ASME Transactions on Mechatronics.